

Construction of Relative Permeability Curves by Numerical Simulation of Two-Phase Flow in 3D CT-Models

Tatyana Khachkova[1(✉)] and Vadim Lisitsa[2]

[1] Institute of Petroleum Geology and Geophysics SB RAS, Koptug Avenue 3, Novosibirsk 630090, Russia
khachkovats@ipgg.sbras.ru

[2] Institute of Mathematics SB RAS, Koptug Avenue 2, Novosibirsk 630090, Russia
lisitsavv@ipgg.sbras.ru

Abstract. The paper describes an algorithm for constructing relative phase permeability curves based on a numerical simulation of primary drainage and subsequent water re-saturation. These processes are simulated as two-phase fluid flows in three-dimensional models generated from CT-images. We use the Navier-Stokes equations to simulate the flow and the Cahn-Hilliard equation to model phase transport. In the applied phase field method, phases are specified by a concentration function. This function is smooth so that the interphase boundary is replaced by a fairly thin layer in which the values of the concentration function continuously change. This representation makes it possible to robustly calculate surface tension forces and take into account the contact angle when using the finite difference method for numerical modeling of fluid flows and phase transport.

Keywords: Two-phase flow · Phase field method · Relative phase permeability · CT-images

1 Introduction

One of the main directions in developing digital rock physics is the simulation of fluid flows at the pore scale. It is due to high interest from industry since the estimates of rock permeability, both absolute and relative, are key parameters in hydrodynamic modeling and optimization of hydrocarbon reservoir development processes.

The simplest task is the simulation of one-phase flow to estimate absolute permeability based on solving the stationary Stokes equation in pore space [1,3]. At the same time, assessments of relative phase permeability, residual oil and water saturation, as well as the construction of relative permeability curves and capillary pressure curves, require solving a much more complex problem, namely,

This study was funded by Russian Science Foundation (grant no. 21-71-20003).

© The Author(s), under exclusive license to Springer Nature Switzerland AG 2024
O. Gervasi et al. (Eds.): ICCSA 2024 Workshops, LNCS 14817, pp. 250–262, 2024.
https://doi.org/10.1007/978-3-031-65238-7_17

the simulation of multi-phase flows in pore space with complex topology. The main problem of such modeling is considering the moving phase boundary. There are several approaches to solving this problem, for example, direct edge tracking methods [6], level-set method [5,11], phase field method [4,9,14] and others. The first technique is difficult to carry out in the three-dimensional case, particularly in regions with complicated topology. Direct tracking of the boundary requires separate consideration of each event where a droplet separates from the general flow, division of the interface into several, and so on. The second method implicitly defines an interface as the zero level of a function that specifies a signed distance. It enables the handling of complicated geometry in the computational domain. However, the numerical error in the solution obtained by this method manifests itself in a nonphysical change in the volume of the phases, which requires further regularization [7,13]. In addition, the surface tension forces arising at the interface depend on the curvature of this interface, which requires calculating the second derivative of this surface. In the case where it is specified by the level-set method, such calculations are subject to a high level of numerical error. Moreover, approximating the contact angle condition is also difficult for this method. The phase field method uses a diffuse interface technique, in which the phase boundary is smoothed over several grid cells. As a result, the concentration function becomes sufficiently smooth to be approximated by mesh functions used in finite volume, finite difference, or finite element methods [9]. In such a mathematical model, fluid flow satisfies the Navier-Stokes equation with variable fluid density and viscosity, and phase transport (concentration function) satisfies the fourth-order Cahn-Hilliard equation with nonlinear terms. Undoubtedly, such an equation goes beyond the classical theory of equations of mathematical physics, but it can be solved quite effectively using the finite difference method. Moreover, this approach is applicable for calculating flows in domains with complex topology, i.e., in the pore space of rocks.

Section 2 presents a system of Navier-Stokes-Cahn-Hilliard equations for describing two-phase fluid flows in domains with complex geometry. For this system, an explicit finite-difference approximation is given (Sect. 3), which makes it possible to calculate the solution using modern computing systems. After that, we present the algorithm for constructing the relative permeability curves. We numerically simulate the primary drainage (Sect. 4.1) with the subsequent waterflooding (Sect. 4.2). The results of numerical experiments are provided for the sandstone sample from the Bentheimer outcrop.

2 Statement of the Problem

In this study, we build a model using segmented microtomographic images of rock [2]. In such a model, a value of one corresponds to the pore space, and zero corresponds to the rock matrix. It is assumed that the rock is monomineral, which implies a constant contact angle, but the approach can be easily generalized to the case of polymineral rock. Formally, we can consider the domain (sample) $\Omega = [0; L_1] \times [0, L_2] \times [0, L_3]$, where L_j is the length of the sample in

the direction x_j, $j = 1, 2, 3$. Two non-overlapping subregions are distinguished in this domain: the impermeable rock matrix Ω_s and the pore space Ω_p. Next, it is necessary to introduce the boundaries of the computational domain, making it possible to specify their boundary conditions. Firstly, Γ denotes the interface between the pore space and the rock matrix. Secondly, Γ_b are the sides of the sample: $x_2 = 0$, $x_2 = L_2$, $x_3 = 0$, $x_3 = L_3$. These boundaries can be permeable or completely impenetrable, depending on the formulation of the problem. For this work, they are assumed to be impenetrable to correspond to laboratory experiments measuring permeability. It is also assumed that the contact angles at the boundaries Γ and Γ_b coincides. Thirdly, the next boundaries are introduced: Γ_{in} for an inlet, corresponding to $x_1 = 0$, and Γ_{out} for an outlet, $x_1 = L_1$, through which the fluid flow is maintained.

Fluid flow in the pore space is described by the Stokes equation, in which the nonlinear term is neglected due to the low flow velocity:

$$\begin{aligned} &\frac{\partial \rho(\psi)\vec{u}}{\partial t} = -\nabla p + 2\nabla \cdot (\nu \epsilon(\vec{u})) + \vec{G}(\psi), \\ &\nabla \cdot (\vec{u}) = 0. \end{aligned} \tag{1}$$

In these equations, $\rho(\psi)$ is the density of the fluid, which depends on a specific phase, $\vec{u}$ is the velocity vector, p is the pressure, $\nu(\psi)$ is the viscosity of the fluid, which also depends on the phase, $2\epsilon(u) = \nabla\vec{u} + \nabla\vec{u}^T$ is doubled strain tensor, and $\vec{G}(\psi)$ are external forces. Here, it is assumed that gravitational forces can be neglected so that external forces are due only to interfacial surface tension.

Phase transport satisfies the Cahn-Hilliard equation [9]:

$$\begin{aligned} &\frac{\partial \psi}{\partial t} + \vec{u} \cdot \nabla \psi = \nabla \cdot (M(\psi) \nabla \mu), \\ &\mu = F'(\psi) - \varepsilon^2 \Delta \psi. \end{aligned} \tag{2}$$

Here, $\psi \in [0, 1]$ is the order parameter that defines a specific phase, μ is the chemical potential (auxiliary variable), M is the mobility, which is usually chosen as a constant, ε is the auxiliary parameter that determines the width of the diffuse interfacial boundary. This parameter must be proportional to the square of the grid step. The potential $F(\psi)$ is determined as

$$F'(\psi) = 2\psi(\psi - 1)(2\psi - 1).$$

Several models can represent external forces caused by interfacial surface tension, but within the context of this work, the following relationship is considered:

$$\vec{G}(\psi) = -\frac{6\sqrt{2}}{\varepsilon}\psi \nabla \mu. \tag{3}$$

It is also necessary to introduce the boundary conditions:

$$\begin{aligned} &\vec{u} = 0, \quad \nabla\mu \cdot \vec{n} = 0, \nabla\psi \cdot \vec{n} = -\frac{\sqrt{2}}{\varepsilon}(\psi^2 - \psi)\cos(\theta), && \vec{x} \in \Gamma_b \cup \Gamma, \\ &p = p_{out}, \nabla\mu \cdot \vec{n} = 0, \nabla\psi \cdot \vec{n} = 0, && \vec{x} \in \Gamma_{out}, \\ &q = q_{in}, \quad \nabla\mu \cdot \vec{n} = 0, \psi = \Psi_{in}, && \vec{x} \in \Gamma_{in}. \end{aligned} \tag{4}$$

The first line of conditions is established at impermeable boundaries, ensuring fluid adhesion (velocity equal to zero) and a contact angle equal to θ for the first

phase ($\psi = 1$). The second line of condition, at the outlet, allows the phase to flow freely out and fixes the pressure on the right side of the sample. The third line determines the fluid flow rate on the left side of the sample and sets the phase distribution at the inlet. The initial conditions are assumed to be given; the distribution $\psi(0, \vec{x})$ is given.

3 Finite Difference Approximation

To describe the approximation for the system of Eqs. (1), (2), first, it is convenient to consider a semi-discrete formulation, in which discretization is carried out only in time. In this case, an explicit finite-difference scheme of the first order of approximation in time is used, and the solution to the Navier-Stokes equation is calculated using the projection method. Then, the finite-difference scheme has the form:

$$\begin{aligned}
&\rho(\psi^n)\tfrac{\vec{u}^{n+1/2}-\vec{u}^n}{\tau} = 2\nabla\cdot(\nu(\psi^n)\epsilon(\vec{u}^n)) + \vec{G}(\psi^n),\\
&\nabla\cdot\left(\tfrac{1}{\rho(\psi^n)}\nabla p^{n+1}\right) = \tfrac{1}{\tau}\nabla\cdot\vec{u}^{n+1/2},\\
&\rho(\psi^n)\tfrac{\vec{u}^{n+1}-\vec{u}^{n+1/2}}{\tau} = \nabla p^{n+1},\\
&\tfrac{\psi^{n+1}-\psi^n}{\tau} + \vec{u}^{n+1}\cdot\nabla\psi^n = M\Delta\mu^n,\\
&\mu^n = F'(\psi^n) - \varepsilon^2\Delta\psi^n,
\end{aligned} \tag{5}$$

where τ is the time step of the scheme. It is clear from this representation that all variables except pressure are calculated explicitly, and it is necessary to solve the Poisson equation to determine the pressure on a new layer. To solve it, we use the method of biconjugate gradients with a pseudo-spectral preconditioner, presented in work [8].

Constructing an approximation in space requires introducing staggered grids such that the pressure and order parameter are defined in nodes with integer indices $p_{ijk} = p((x_1)_i, (x_2)_j, (x_3)_k)$ and $\psi_{ijk} = \psi((x_1)_i, (x_2)_j, (x_3)_k)$, and the velocity components are defined in nodes with one half-integer index, i.e., $(u_1)_{i+1/2jk} = u_1((x_1)_{i+1/2}, (x_2)_j, (x_3)_k)$, $(u_2)_{ij+1/2k} = u_2((x_1)_i, (x_2)_{j+1/2}, (x_3)_k)$, $(u_3)_{ijk+1/2} = u_3((x_1)_i, (x_2)_j, (x_3)_{k+1/2})$. Then, the finite-difference scheme will look like this:

$$\begin{aligned}
&\rho\left(\hat{\psi}^n_{i+1/2jk}\right)\tfrac{(u_1)^{n+1/2}_{i+1/2jk}-(u_1)^n_{i+1/2jk}}{\tau} = 2\sum_{m=1}^{3} D_m[\nu(\hat{\psi})\epsilon_{1m}]^n_{i+1/2jk} + G_1(\hat{\psi}^n_{i+1/2jk}),\\
&\rho\left(\hat{\psi}^n_{ij+1/2k}\right)\tfrac{(u_2)^{n+1/2}_{ij+1/2k}-(u_2)^n_{ij+1/2k}}{\tau} = 2\sum_{m=1}^{3} D_m[\nu(\hat{\psi})\epsilon_{2m}]^n_{ij+1/2k} + G_2(\hat{\psi}^n_{ij+1/2k}),\\
&\rho\left(\hat{\psi}^n_{ijk+1/2}\right)\tfrac{(u_3)^{n+1/2}_{ijk+1/2}-(u_3)^n_{ijk+1/2}}{\tau} = 2\sum_{m=1}^{3} D_m[\nu(\hat{\psi})\epsilon_{3m}]^n_{ijk+1/2} + G_3(\hat{\psi}^n_{ijk+1/2}),
\end{aligned} \tag{6}$$

$$
\begin{aligned}
&(\nu(\hat{\psi})\epsilon_{11})^n_{ijk} = \nu(\hat{\psi}^n_{ijk}) D_1[u_1]^n_{ijk},\\
&(\nu(\hat{\psi})\epsilon_{22})^n_{ijk} = \nu(\hat{\psi}^n_{ijk}) D_2[u_2]^n_{ijk},\\
&(\nu(\hat{\psi})\epsilon_{33})^n_{ijk} = \nu(\hat{\psi}^n_{ijk}) D_3[u_3]^n_{ijk},\\
&(\nu(\hat{\psi})\epsilon_{23})^n_{ij+1/2k+1/2} = \tfrac{1}{2}\nu(\hat{\psi}^n_{ij+1/2k+1/2}) \left(D_3[u_2]^n_{ij+1/2k+1/2} + D_2[u_3]^n_{ij+1/2k+1/2}\right),\\
&(\nu(\hat{\psi})\epsilon_{13})^n_{i+1/2jk+1/2} = \tfrac{1}{2}\nu(\hat{\psi}^n_{i+1/2jk+1/2}) \left(D_3[u_1]^n_{i+1/2jk+1/2} + D_1[u_3]^n_{i+1/2jk+1/2}\right),\\
&(\nu(\hat{\psi})\epsilon_{12})^n_{i+1/2j+1/2k} = \tfrac{1}{2}\nu(\hat{\psi}^n_{i+1/2j+1/2k}) \left(D_1[u_2]^n_{i+1/2j+1/2k} + D_2[u_1]^n_{i+1/2j+1/2k}\right),\\
&\sum_{m=1}^{3} Q_m[p,\rho(\psi)]^{n+1}_{ijk} = \tfrac{1}{\tau}\sum_{m=1}^{3} D_m[u_m]^{n+1/2}_{ijk},\\
&\rho\left(\hat{\psi}^n_{i+1/2jk}\right)\tfrac{(u_1)^{n+1}_{i+1/2jk} - (u_1)^{n+1/2}_{i+1/2jk}}{\tau} = D_1[p]^{n+1}_{i+1/2jk},\\
&\rho\left(\hat{\psi}^n_{ij+1/2k}\right)\tfrac{(u_2)^{n+1}_{ij+1/2k} - (u_2)^{n+1/2}_{ij+1/2k}}{\tau} = D_2[p]^{n+1}_{ij+1/2k},\\
&\rho\left(\hat{\psi}^n_{ijk+1/2}\right)\tfrac{(u_3)^{n+1}_{ijk+1/2} - (u_3)^{n+1/2}_{ijk+1/2}}{\tau} = D_3[p]^{n+1}_{ijk+1/2},\\
&\mu^n_{ijk} = 2\psi^n_{ijk}(\psi^n_{ijk}-1)(2\psi^n_{ijk}-1) - \varepsilon^2\sum_{m=1}^{3} D^2_m[\psi]^n_{ijk},\\
&\tfrac{\psi^{n+1}_{ijk} - \psi^n_{ijk}}{\tau} + \sum_{m=1}^{3} D^F_m[u^{n+1}_m \psi^n]_{ijk} = M\sum_{m=1}^{3} D^2_m[\mu]^n_{ijk}.
\end{aligned}
\tag{7}
$$

In this notation, finite-difference operators have the following form:

$$
\begin{aligned}
&D^2_1[q]^n_{IJK} = \tfrac{q^n_{I+1JK} - 2q^n_{IJK} + q^n_{I-1JK}}{h_1^2},\\
&Q_1[p,\rho(\psi)]^{n+1}_{ijk} = \tfrac{1}{h_1}\left(\tfrac{1}{\hat{\rho}(\psi^n_{i+1/2jk})}\tfrac{p^{n+1}_{i+1jk} - p^{n+1}_{ijk}}{h_1} - \tfrac{1}{\hat{\rho}(\psi^n_{i-1/2jk})}\tfrac{p^{n+1}_{ijk} - p^{n+1}_{i-1jk}}{h_1}\right),\\
&D_1[q]^N_{IJK} = \tfrac{q^N_{I+1/2JK} - q^N_{I-1/2JK}}{h_1},\\
&D^F_1[u^{n+1}_1\psi^n]_{ijk} = \tfrac{F^1_{i+1/2jk} - F^1_{i-1/2jk}}{h_1},\\
&F^1_{i+1/2jk} = \begin{cases} (u_1)^{n+1}_{i+1/2jk}\psi^n_{i+1jk}, & (u_1)^{n+1}_{i+1/2jk} < 0,\\ (u_1)^{n+1}_{i+1/2jk}\psi^n_{ijk}, & (u_1)^{n+1}_{i+1/2jk} > 0. \end{cases}
\end{aligned}
\tag{8}
$$

Here h_1 is the grid step in the direction x_1. Indices written in lowercase letters can only take integer values, while capital letters imply that they can be either whole or half-integer values. Operators that approximate derivatives with respect to two other spatial coordinates can be obtained by appropriate substitution of indices. It should be noted that the resulting difference scheme provides first-order approximation in time and space. In this case, the order of approximation in space can be increased using more accurate schemes for approximating phase transport. Currently, the simplest upwind scheme is used for this purpose, but it can be replaced by a third-order WENO scheme [10,12]. Note, that components of the strain tensor (7) are not computed or stored explicitly in real simulations, but they are substituted to the Eqs. (6). However, for the sake of simplicity we provide the Eqs. (6) and (7) separately.

The described algorithm's implementation is focused on using graphic co-processors. Explicit schemes are used at all stages except for solving the Poisson equation. They are easily implemented on CUDA. The algorithm presented in [8] is used to solve the Poisson equation.

4 Numerical Experiments

In our numerical experiments we use the CT-scans of a sandstone sample from the Bentheimer outcrop with the size of 200^3 voxels and the resolution of 1.72 μm per voxel. In our work [3], we investigated the influence of the scale of a digital image of a rock, that is, its size and resolution, on the assessment of various parameters, particularly transport parameters. We followed the definition of statistically representative volume, or SREV, presented in [15]: a volume is statistically representative if the variance of the property being valued does not exceed a certain level (say, 10%) of its average value for all statistically equivalent measurements. Based on this definition, the representative size for transport parameters was shown to be larger than what we had available. However, the calculated estimates were quite close to the values obtained in the laboratory. In this work, we used a digital sample, which is also not representative (according to the specified criterion) for assessing transport parameters. However, the absolute permeability calculated using the above approach is also close to the laboratory one. Therefore, this sample is used to represent the algorithm for constructing relative permeability curves.

We numerically simulate a steady-state laboratory method for measuring relative permeability to construct such curves. The first step of this method is to saturate the rock sample with 100% water and measure the absolute permeability. In the second step, only oil is injected into the sample until a steady-state regime is achieved, after which the irreducible water saturation and the maximum oil relative permeability are measured. This process is called primary drainage. Next, both fluids are injected in different ratios, with the amount of water being minimal at first. For each subsequent experiment, the proportion of water gradually increases until 100% water is reached. For each experiment and subsequent measurements, it is necessary to establish a steady-state mode. The described process is called waterflooding (or water re-saturation, inhibition). Let us describe in detail the numerical modeling of these processes.

4.1 Numerical Simulation of Primary Drainage

Under natural conditions, a reservoir, initially completely saturated with water, is gradually filled with oil, which migrates from the source rock. Numerical simulation of drainage, in which the wetting phase (water in case of water-wet system) decreases, repeats this process, i.e., oil is injected into a rock sample completely filled with water. It is done until the oil displaces all possible water so that irreducible water saturation is reached. It is the moment when a reservoir is discovered in nature, and at this time, the oil's relative permeability is the maximum. In contrast, the water's relative permeability becomes equal to zero. These are the endpoints of the drainage relative permeability curves and the starting points of the waterflooding relative permeability curves. The second set of curves is significant for the petroleum industry; we will describe their construction in the following subsections.

When simulating drainage, we use the following parameters: sample size is 200^3 voxels, porosity is $\phi = 21.2\%$, mesh spacing is $1.75 * 10^{-6}$ m, water and oil density are $\rho = [1000; 880]$ kg/m^3, fluids viscosity $\nu = [3.8 * 10^{-4}; 4.027 * 10^{-3}]$ Pa $\cdot$ s, interfacial tension $\sigma = 2.571 * 10^{-2}$ N/m, contact angle for the first fluid (water) $\theta = 38.7°$. We specify the flow velocity at the inlet $v = 1 * 10^{-1}$ m/s and the time required to reach steady-state $T = 3.7 * 10^{-3}$ s. During this time, five volumes of pore space will pass through the sample. The calculated time step is approximately $\tau = 1.00385 * 10^{-8}$ s. In addition, we define the water/oil ratio for the injected mixture as the ratio of the water volume to the total volume. In the case of drainage, this ratio is equal to 0 since only oil is injected.

We perform three numerical experiments simulating flow in three spatial directions. During the experiments, we record the distribution of the phase field, pressure, and velocity at each point of the digital sample for certain points in time. From the data obtained, we can calculate the resulting water saturation, as well as the effective and relative permeabilities. The last parameters are determined from the following relations:

$$k_w = \frac{q_w \nu_w L}{A \Delta P_w}, \; k_o = \frac{q_o \nu_o L}{A \Delta P_o}, \; k_{rw} = \frac{k_w}{k}, \; k_{ro} = \frac{k_o}{k}, \tag{9}$$

where k_w, k_o are the effective water and oil permeabilities, q_w, q_o are water and oil flow rates, ν_w, ν_o are fluid viscosities, L is the sample length, A is cross-sectional area, $\Delta P_w, \Delta P_o$ are the pressure drops, k_{rw}, k_{ro} are the relative water and oil permeabilities and k is the absolute permeability.

Figure 1 illustrates the described simulation of the drainage process for a sandstone sample from the Bentheimer outcrop.

4.2 Numerical Simulation of Water Re-saturation

At a certain stage of oil field development, the need arises for forced injection of water into the reservoir. It is done in order to displace oil from it. At this stage, it is necessary to have waterflooding relative permeability curves to predict fluid behavior and provide the most efficient hydrocarbon production.

In the steady-state laboratory method for measuring relative permeability, the water re-saturation is the third step, following the drainage. Here, both fluids are simultaneously injected into the sample in a certain ratio; then, the experimenter waits for the steady-state regime to be established, after which the parameters are measured, and the next points on the relative permeability curves are calculated. Each laboratory experiment can take several hours to several days depending on the absolute permeability, i.e., this method is very time-consuming. However, it is considered more accurate than the displacement method, in which only water is pumped, and which requires analytical interpretation of the results.

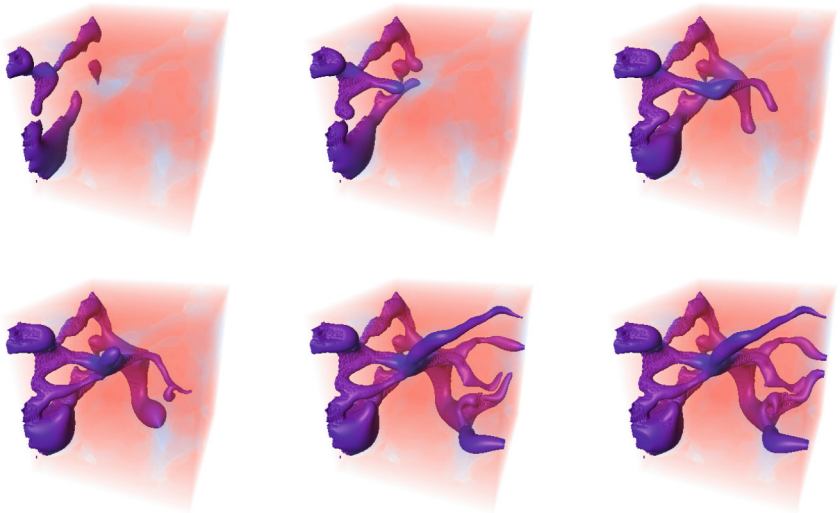

Fig. 1. The relative arrangement of phases (water has a blue translucent color, oil has a lilac color) in the pore space when water is displaced by oil at different points in time. (Color figure online)

To numerically simulate the waterflooding process we, just like in the laboratory, perform a series of experiments. In the first numerical experiment, the proportion of water in the injected fluid mixture is minimal, for example, 0.1, 0.05, or 0.025; in each subsequent experiment, this proportion increases. It continues until only water is injected, i.e. its ratio to the total volume will reach 1. As at the drainage simulation, the phase field, pressure, and velocity distribution are recorded during experiments, from which the water saturation, effective, and relative permeabilities are then calculated using formulas (9). The results obtained are added to the curves. The smaller the step in the water fraction, the more accurate the curves should be. Additionally, we perform this numerical simulation in two different ways. In the first, we simultaneously generate models for all experiments of the first series, starting with the model of the drainage stage, changing only the proportion of water in the mixture, and calculating the results of all experiments in this series in parallel. In the second way, we perform all experiments sequentially, i.e., the model obtained in the previous step is used for the next calculation, in which the proportion of injected water is also increased. The second approach requires more time and effort, so testing whether it gives more accurate results than the first is necessary.

Figures 2, 3 illustrate the described simulation of the water re-saturation process for the sandstone sample. Figure 2 shows that with a water fraction in the mixture of 0.1, 0.3, and 0.6, the oil remains in the system, but different parts of it are replaced by the water.

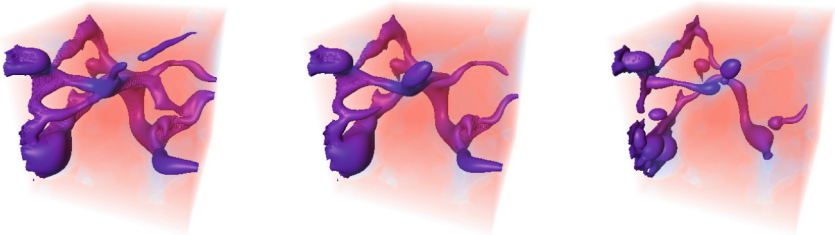

Fig. 2. The relative arrangement of phases (water has a blue translucent color, oil has a lilac color) in the pore space after the waterflooding, the proportions of injected water in the mixture are 0.1, 0.3, 0.6 for images from left to right. (Color figure online)

Figure 3 shows how, with a water fraction of 1, i.e., when only water is injected into the sample, the oil is almost completely replaced by water during the waterflooding process. It is the last experiment in each series, and as a result, the oil's relative permeability becomes zero, and the residual oil saturation is determined from the corresponding calculated water saturation value.

As in laboratory steady-state experiments, to determine the relative permeabilities, it is necessary to wait until a steady-state regime is established; also, in numerical experiments, we wait until the calculated values (the water saturation and the phase permeabilities) are established. Figures 4, 5 show how the process of establishing these values occurs. Figure 4 shows how water saturation gradually increases when injecting a mixture with a water ratio of 0.8. At approximately the 30th snap out of 100, the value reaches a plateau, and starting from the 50th snap, it practically does not deviate from the average value calculated for the snaps 50–100. The values of effective permeabilities for water and oil behave similarly. Figure 5 shows that the values approach the average (calculated for the last 50 steps) approximately at the 20th snap. After the 50th snap, they practically do not differ from this average.

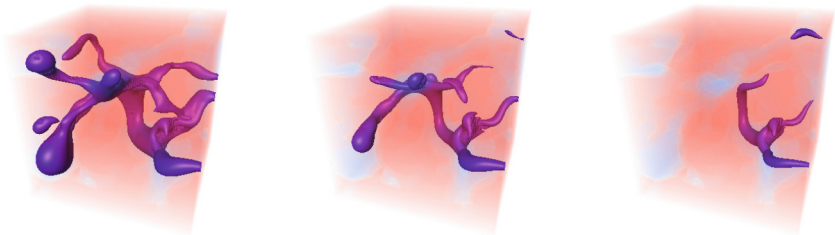

Fig. 3. The relative arrangement of phases (water has a blue translucent color, oil has a lilac color) in the pore space during the last waterflooding experiment, when only the water is injected into the system, at different times. (Color figure online)

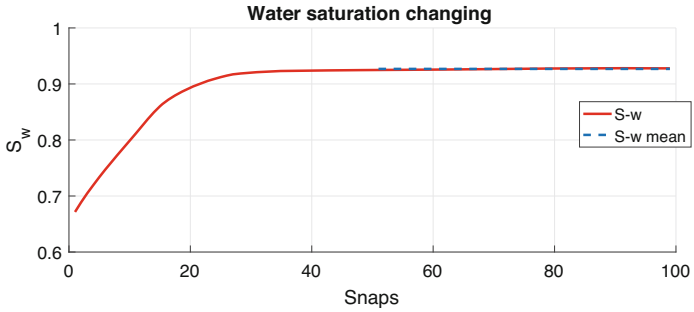

Fig. 4. Water saturation depending on the time of the experiment; a mixture with a water ratio of 0.8 is injected into the sample. The mean value calculated for the snaps 50–100 is shown with a dashed blue line. (Color figure online)

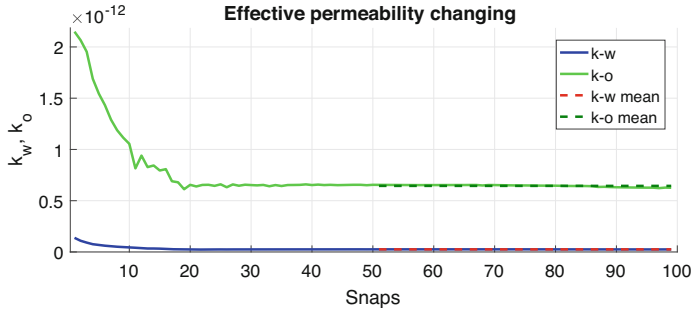

Fig. 5. Water and oil effective permeabilities depending on the time of the experiment. The mean values calculated for the snaps 50–100 are shown with dashed red and dark green lines. (Color figure online)

4.3 Effective and Relative Permeabilities Curves

To construct the effective and relative permeability curves, we first numerically simulate the drainage, resulting in the first points of each graph; after that, we simulate the waterflooding and calculate the next 10 points corresponding to water-to-total mixture ratios from 0.1 to 1.

We perform numerical experiments in three different spatial directions: x, y, and z. As already mentioned, two series for the waterflooding are performed for all directions: parallel calculations and sequential ones. Thus, we obtain four effective and relative permeability curves for each direction (two for water and two for oil). In Figs. 6, 7, dashed lines with the triangle points indicate curves obtained by a fast parallel method (first series), and solid lines with the star points indicate curves obtained by a sequential method (second series) when the model from the previous experiment is used for the subsequent one. The legend shows the correspondence of the graphs to the directions.

Figures 6, 7 show that the results of the two series are very close to each other, but the graphs for the second series are slightly smoother. Thus, if we

need to perform calculations quickly, we can use the first method, i.e., perform all calculations simultaneously. If we want to get more accurate results, it is better to perform all experiments sequentially, one after another.

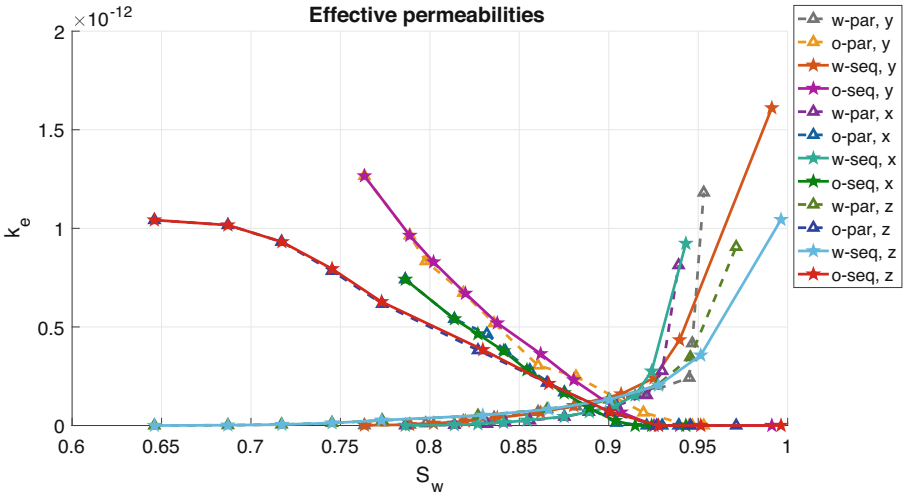

Fig. 6. Effective permeabilities curves for the Bentheimer sandstone sample for various spacial directions. The results of the first experiment series are shown by the dashed lines, and the solid lines show the results of the second series.

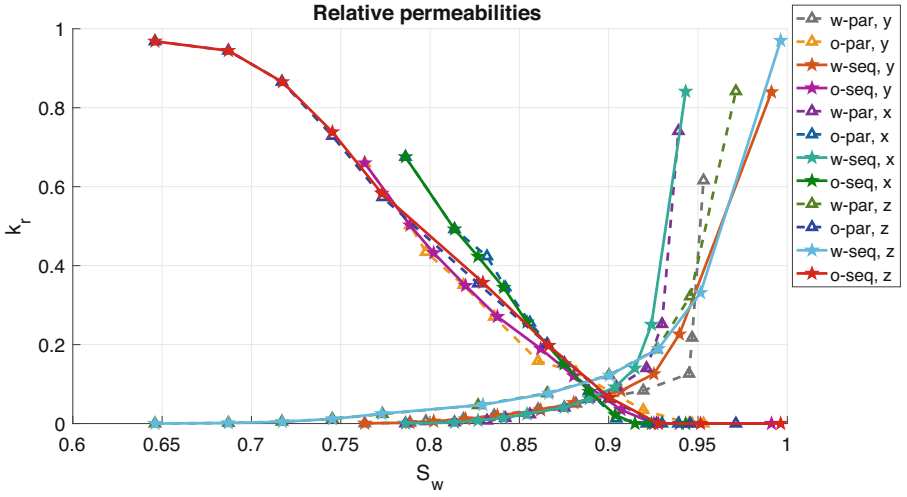

Fig. 7. Relative permeabilities curves for the Bentheimer sandstone sample for different spacial directions. The results of the first experiment series are shown by the dashed lines, and the solid lines show the results of the second series.

5 Conclusion

In this paper, we describe the numerical algorithm for constructing the relative phase permeability curves in a non-destructive way using the CT-images of rock samples. In our case, the rock is mono-mineral, but the approach can be easily generalized to the case of a poly-mineral rock. In the algorithm presented, we numerically simulate a steady-state laboratory method for measuring relative permeability. This laboratory method is very time-consuming but produces accurate results. Following this method, we numerically simulate the primary drainage and subsequent water re-saturation as two-phase fluid flows in three-dimensional models. We use the Navier-Stokes equations to simulate the flow and the Cahn-Hilliard equation to model phase transport. In the applied phase field method, phases are specified by a concentration function. This function is smooth so that the interphase boundary is replaced by a fairly thin layer in which the values of the concentration function continuously change. This representation makes it possible to robustly calculate surface tension forces and take into account the contact angle when using the finite difference method for numerical modeling of fluid flows and phase transport. Moreover, this approach is applicable for calculating flows in domains with complex topology, i.e., in the pore space of rocks.

All numerical experiments were performed on a sandstone sample from the Bentheimer outcrop. When simulating waterflooding, we conducted two series of experiments. All experiments were calculated in parallel in the first fast series, with the same model (obtained after drainage) but with different water ratios in the injected mixture. The experiments of the second series were carried out sequentially, one after another. The model from the previous experiment was used for the next one, and the water ratios were also changed. A comparison of the results of the two series showed that the obtained relative permeability curves are very close to each other, but the curves constructed during the second series are slightly smoother.

Thus, if we need to perform calculations quickly and for a larger number of points, it is better to use the first method, i.e. perform all calculations simultaneously. If we want to get more accurate results, it is better to carry out all experiments sequentially, one after another. However, this will require significantly more time and effort. Despite this, the numerical method is still less time-consuming than the laboratory one.

References

1. Andra, H., et al.: Digital rock physics benchmarks - Part I: imaging and segmentation. Comput. Geosci. **50**, 25–32 (2013)
2. Andra, H., et al.: Digital rock physics benchmarks - Part II: computing effective properties. Comput. Geosci. **50**, 33–43 (2013)
3. Bazaikin, Y., et al.: Effect of CT image size and resolution on the accuracy of rock property estimates. J. Geophys. Res. Solid Earth **122**(5), 3635–3647 (2017)

4. Boyer, F., Lapuerta, C., Minjeaud, S., Piar, B., Quintard, M.: Cahn-Hilliard/Navier-stokes model for the simulation of three-phase flows. Transp. Porous Media **82**(3), 463–483 (2010)
5. Gibou, F., Fedkiw, R., Osher, S.: A review of level-set methods and some recent applications. J. Comput. Phys. **353**, 82–109 (2018)
6. Groot, R.D.: Second order front tracking algorithm for Stefan problem on a regular grid. J. Comput. Phys. **372**, 956–971 (2018). https://doi.org/10.1016/j.jcp.2018.04.051
7. Jettestuen, E., Friis, H.A., Helland, J.O.: A locally conservative multiphase level set method for capillary-controlled displacements in porous media. J. Comput. Phys. **428**, 109965 (2021). https://doi.org/10.1016/j.jcp.2020.109965
8. Khachkova, T., Lisitsa, V., Reshetova, G., Tcheverda, V.: GPU-based algorithm for evaluating the electrical resistivity of digital rocks. Comput. Math. Appl. **82**, 200–211 (2021)
9. Kim, J.: Phase-field models for multi-component fluid flows. Commun. Comput. Phys. **12**(3), 613–661 (2012)
10. Luo, K., Zhuang, Z., Fan, J., Haugen, N.E.L.: A ghost-cell immersed boundary method for simulations of heat transfer in compressible flows under different boundary conditions. Int. J. Heat Mass Transf. **92**, 708–717 (2016)
11. Osher, S., Fedkiw, R.P.: Level set methods: an overview and some recent results. J. Comput. Phys. **169**(2), 463–502 (2001)
12. Prokhorov, D., Lisitsa, V., Khachkova, T., Bazaikin, Y., Yang, Y.: Topology-based characterization of chemically-induced pore space changes using reduction of 3d digital images. J. Comput. Sci. **58**, 101550 (2022)
13. Sussman, M., Fatemi, E.: An efficient, interface-preserving level set redistancing algorithm and its application to interfacial incompressible fluid flow. SIAM J. Sci. Comput. **20**(4), 1165–1191 (1999)
14. Yang, J., Kim, J.: A novel Cahn-Hilliard-Navier-stokes model with a nonstandard variable mobility for two-phase incompressible fluid flow. Comput. Fluids **213**, 104755 (2020). https://doi.org/10.1016/j.compfluid.2020.104755
15. Zhang, D., Zhang, R., Chen, S., Soll, W.E.: Pore scale study of flow in porous media: scale dependency, rev, and statistical rev. Geophys. Res. Lett. **27**(8), 1195–1198 (2000)